Optimized image acquisition for dopamine transporter imaging with ultra-high resolution clinical pinhole SPECT

Chen, Yuan; Vastenhouw, Brendan; Wu, Chao; Goorden, Marlies C.; Beekman, Freek J.

DOI
10.1088/1361-6560/aae76c

Publication date
2018

Document Version
Final published version

Published in
Physics in Medicine and Biology

Citation (APA)
Chen, Y., Vastenhouw, B., Wu, C., Goorden, M. C., & Beekman, F. J. (2018). Optimized image acquisition for dopamine transporter imaging with ultra-high resolution clinical pinhole SPECT. *Physics in Medicine and Biology*, *63*(22). https://doi.org/10.1088/1361-6560/aae76c

Physics in Medicine & Biology

IPEM Institute of Physics and Engineering in Medicine

PAPER

Optimized image acquisition for dopamine transporter imaging with ultra-high resolution clinical pinhole SPECT

To cite this article: Yuan Chen *et al* 2018 *Phys. Med. Biol.* **63** 225002

Recent citations

- Performance evaluation of a novel multi-pinhole collimator for dopamine transporter SPECT
  K Tecklenburg *et al*
- Optimized sampling for high resolution multi-pinhole brain SPECT with stationary detectors
  Yuan Chen *et al*
- Primary, scatter, and penetration characterizations of parallel-hole and pinhole collimators for I-123 SPECT
  Arda Könik *et al*

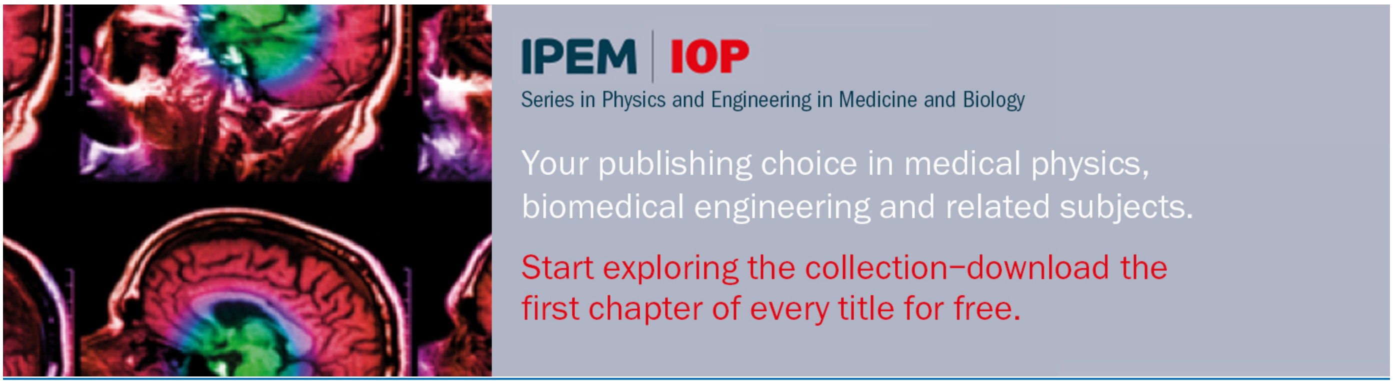

IOP Publishing Phys. Med. Biol. 63 (2018) 225002 (17pp) https://doi.org/10.1088/1361-6560/aae76c

Physics in Medicine & Biology

IPEM Institute of Physics and Engineering in Medicine

CrossMark

RECEIVED
25 January 2018

REVISED
1 August 2018

ACCEPTED FOR PUBLICATION
10 October 2018

PUBLISHED
7 November 2018

PAPER

Optimized image acquisition for dopamine transporter imaging with ultra-high resolution clinical pinhole SPECT

Yuan Chen[1], **Brendan Vastenhouw**[2,3], **Chao Wu**[1,2,3], **Marlies C Goorden**[1] and **Freek J Beekman**[1,2,3]

[1] Section Biomedical Imaging, Delft University of Technology, Delft, Netherlands
[2] MILabs B.V., Utrecht, Netherlands
[3] Department of Translational Neuroscience, Brain Center Rudolf Magnus, University Medical Center Utrecht, Utrecht, Netherlands

E-mail: y.chen-4@tudelft.nl

Keywords: DaTscan, clinical SPECT, sampling, brain imaging, high resolution SPECT, high sensitivity SPECT, pinhole collimator

Abstract

SPECT can be used to image dopamine transporter (DaT) availability in the human striatum, e.g. for diagnosis of Parkinson's disease (PD). As traditional SPECT provides limited resolution and sensitivity, we proposed a full ring focusing multi-pinhole SPECT system (G-SPECT-I (Beekman 2015 *Eur. J. Nucl. Med. Mol. Imaging* **42** S209)) which demonstrated a 2.5 mm reconstructed resolution in phantom scans. G-SPECT-I achieves data completeness in the scan region of interest by translating the patient bed with an *xyz*-stage and combining projections from all bed positions into image reconstruction using a scanning focus method (SFM). This paper aims to develop dedicated SFM parameters for performing a DaTscan with high effective sensitivity and appropriate sampling. To this end, the axial scanning length was restricted and transaxial bed trajectories with a reduced number of positions based on a convex hull data-completeness model were tested. Quantitative accuracy was assessed using full G-SPECT-I simulations of an Alderson phantom based on measured system matrices. For each sampling strategy, the specific binding ratio (SBR) and asymmetry index (AI) in the left and right striatum, as well as the Localized SBR (L-SBR) and the Localized AI (L-AI) in eight striatal sub-regions were calculated and compared to those of the reference scan which performs full brain oversampling using 112 bed positions. Results show that structures essential for PD diagnosis were visually and quantitatively barely affected even when using the lowest number of bed translations (i.e. 4). The maximum deviation from the reference was only 1.5%, 1.5%, 5.5% and 7.0% for the SBR, AI, L-SBR and L-AI, respectively, when 4 positions were used. Thus, it is possible to perform an accurate DaTscan with a confined axial scan region and a limited number of focused bed positions. This enables protocols for extremely fast dynamic SPECT scans with less than half-minute time frames, which can be useful for motion correction.

1. Introduction

SPECT imaging of the dopamine transporter (DaT) density with e.g. ^{123}I-ioflupane has been used as an imaging biomarker for e.g. Parkinson's disease diagnosis and for differentiation of dementia with Lewy Body from other dementias (Catafau and Tolosa 2004, O'Brien *et al* 2004, Hauser and Grosset 2012, Bajaj *et al* 2013, Gayed *et al* 2015). Currently, the diagnosis derived from a DaTscan mainly relies on visual interpretation based on the bilateral striatal shape, the striatal symmetry, the gradient between the two striatal parts (caudate and putamen) and the striatal DaT density (Park 2012). However, conventional dual-head SPECT scanners equipped with low-energy high-resolution (LEHR) parallel hole collimators—the most frequently used collimators for SPECT DaT imaging (Marzullo *et al* 2013, Lee *et al* 2014)—generally provide a limited resolution of about 8–10 mm and a sensitivity of about 70–90 cps/MBq/head (Kouris *et al* 1993, Bombardieri *et al* 2007)). This results in a compromised ability to recover the striatum and to separate putamen and caudate, and demands a long scanning time and/or a relatively high radioactive dose. The development of three-head fan beam SPECT was an attempt to improve the resolution-sensitivity tradeoff by the use of image magnification with converging collimation and the use of more detectors surrounding the patient. While the sensitivity was indeed increased to around

250 cps MBq^{-1} (e.g. GCA-9300A and Prism 3000XP (Kouris *et al* 1993, Kawamura *et al* 2008)), the resolution that was achieved was only slightly improved to about 7 mm (De Deyn 1997, Bombardieri *et al* 2007, Goorden *et al* 2009, Van Audenhaege *et al* 2015). Some dedicated brain SPECT scanners have been developed that strive to achieve a slightly better resolution by either using sophisticated detectors (e.g. Mediso X-Ring/4R), or a large number of focusing collimators and detectors (e.g. NeuroFocus and inSpira HD with a resolution of about 7 mm (Van De Giessen and Booij 2010, Stoddart and Stoddart 1992, Sensakovic *et al* 2013)), yet only few clinical validations with these scanners are available (Van De Giessen and Booij 2010, Tavares *et al* 2013, Dierckx *et al* 2014) and some are not even manufactured anymore. A SPECT system which could achieve a much better resolution-sensitivity tradeoff would be very desirable for its ease of dose requirement and possibility for dynamic scans or longitudinal studies.

Recently, SPECT systems with multi-pinhole collimators are gaining increasing interest owing to their enhanced resolution-sensitivity tradeoff, especially when imaging small objects. Research has been carried out in many groups to improve the performance of brain SPECT by optimizing a multi-pinhole system geometry in simulations (Van Audenhaege *et al* 2011, 2013, Mukherjee *et al* 2014, King *et al* 2016, Chen *et al* 2017). However, to the best of our knowledge, these systems are still in the design phase and few have acquired physical scans. In Lee *et al* (2014), a physical multi-pinhole SPECT system was assembled by mounting 20-multipinhole collimators onto a dual-head conventional SPECT scanner. The authors concluded that with their chosen multi-pinhole collimator, scan time can be shortened by one-third compared to that of a LEHR collimator (20 min against 30 min) while achieving comparable image quality. However, with the big aperture size of 7.5 mm and the small pinhole-detector distance compared to the object-pinhole distance, the authors estimated the resolution of this multi-pinhole SPECT system to be about 20.6 mm.

Our group recently launched a multi-pinhole clinical SPECT system with full angular coverage using stationary detectors, that demonstrates excellent resolution-sensitivity tradeoff (G-SPECT-I (Beekman *et al* 2015)). For objects the size of a human head, unprecedented resolutions and sensitivities were achieved in phantom scans: 2.5 mm resolution with 415 cps MBq^{-1} sensitivity and 3.5 mm resolution with 896 cps MBq^{-1} sensitivity, using 3 mm and 4.5 mm-diameter pinhole collimators, respectively. These collimators contain a total of 54 focusing pinholes and a total of nine large field of view cameras surrounding the patient (figure 1). The geometry is designed such that all pinholes are 'viewing' a central volume, in which a very high sensitivity is obtained over a 360° angular range. This central volume is referred to as the complete data volume (CDV) in subsequent sections, as photons emitted from this volume are captured by all pinholes at different angles and sufficient angular sampling for accurate image reconstruction is attained without any detector rotation or bed shift. For extending the volume from which complete data is obtained, the bed is stepped through the scanner with an automated *xyz*-stage, allowing different parts of the patient to be positioned in the CDV. Projections from all pinholes and all bed positions are then used simultaneously for image reconstruction, a strategy referred to as the scanning focus method (SFM) (Vastenhouw and Beekman 2007). Preclinical applications of a similar design have been successfully applied in U-SPECT$^+$ (Vastenhouw and Beekman 2007, Ivashchenko *et al* 2015a, 2015b) which enables dynamic animal scans with sub-second frame dynamics or extremely low dose scans (fractions of 1 MBq). Hence, it may be possible that the G-SPECT-I technology could bring e.g. dynamic scanning or very low dose (longitudinal) scanning into reach for larger subjects, including patients.

This paper focuses on an optimal application of G-SPECT-I to DaT imaging with high effective sensitivity. It is plausible that this could be achieved by confining the scan to the volume of interest (VOI) in which the striatum locates, such that more gamma photons from the VOI are captured and the effective count yield is increased compared to that for whole brain scanning. Based on the Hammers N30R83 brain atlas (Hammers *et al* 2003) (average over 30 healthy MR scans) and a CT image of the Alderson brain phantom, the axial length of the striatum is estimated to be about 35 mm. Actually, visual inspections and semi-quantitative analyses of DaTscans often only use the three consecutive slices with the highest striatal intensity, which in total measure approximately 10–12 mm axially (Koch *et al* 2005, Acton *et al* 2006, Lange *et al* 2014, Augimeri *et al* 2016). Hence, we aim to ensure an accurately reconstructed region of 35 mm in the axial direction, which should be more than sufficient for DaTscan analysis. However, for a scan confined to only part of the brain it needs to be investigated whether limited sampling and projection truncation in axial direction do induce artefacts. Apart from confining the axial scan region, it is also desirable to optimize the bed translation trajectory on the transaxial plane such that, (i) sufficient sampling on the transaxial plane is ensured to circumvent the interior problem, and (ii) the effective count yield is maximized. The latter can be achieved by placing transaxial bed positions such that they focus more on the striatum and/or by limiting the number of bed positions to reduce the overhead time needed for the bed movements. However, a more focused bed position placement may not cover the entire brain especially the periphery, and scanning with a limited number of bed positions may mean that not every part of the scan region is covered at least once by the CDV. Both could have consequences for data completeness over the VOI and thus have to be investigated in detail.

The aim of this paper is to develop sampling strategies for G-SPECT-I DaT imaging with high effective sensitivity by (i) confining the scan region in the axial direction, and (ii) focusing the bed positions transaxi-

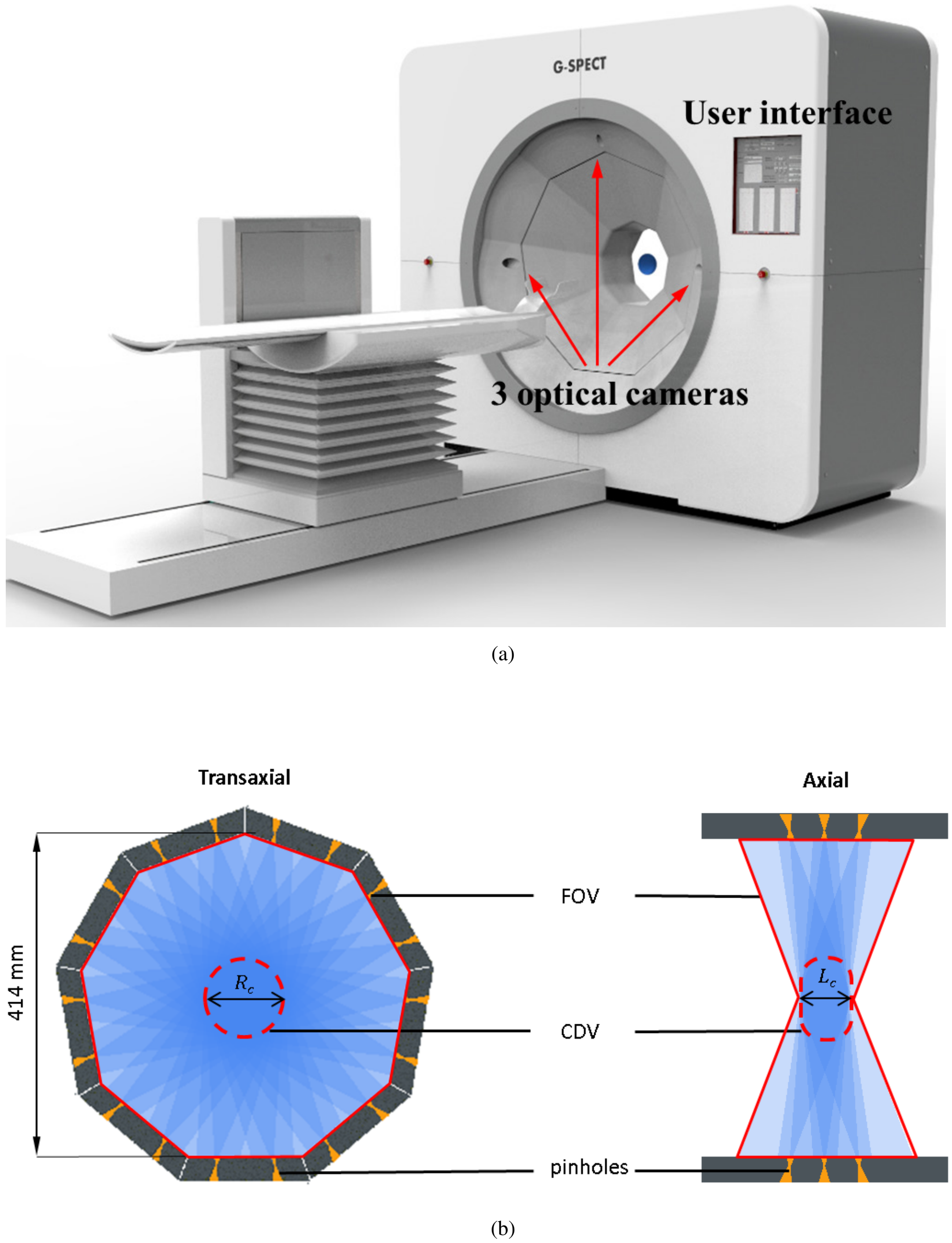

Figure 1. Illustration of G-SPECT-I scanner. (a) G-SPECT-I system with three optical cameras and a user interface for VOI selection; (b) multi-pinhole collimator of G-SPECT-I system. All 54 pinholes distributed over three rings are focusing on the CDV. Pinholes each have an opening angle of 27°, resulting in a CDV with transaxial diameter R_c of 100 mm and axial length L_c of 60 mm.

ally in the brain and limiting the number of transaxial bed positions, while always ensuring sufficient sampling in the transaxial plane. Quantitative accuracy attained with different sampling strategies is assessed using full G-SPECT-I system simulations of an Alderson phantom based on measured system matrices.

2. Methods

2.1. System design and collimator geometry

G-SPECT-I (figure 1) is based on a stationary ring consisting of nine pinhole-collimated gamma cameras with large-area 595 × 472 × 9.5 mm NaI crystals. The interchangeable nonagon-shaped collimator assumed in this paper consists of a total of 54 3 mm-diameter pinhole apertures. Pinholes are placed in three rings with a relative rotation of 1/3 of an inter-pinhole distance in between rings. Pinholes each have an opening angle of 27°, all focusing on the CDV (figure 1). The transaxial diameter R_c and axial length L_c of the CDV are 100 mm and

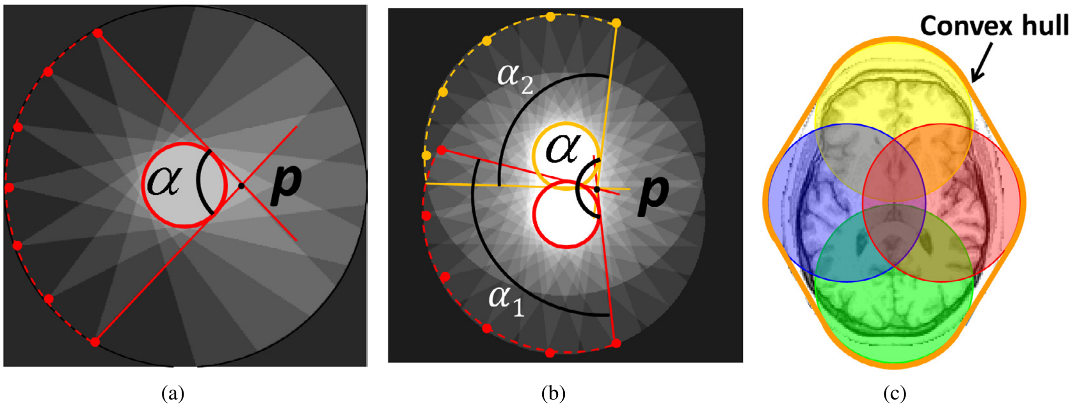

Figure 2. Illustration of convex hull principle in the transaxial plane. The red and yellow circles in (a) and (b) indicate the CDVs. (a) The angular coverage α in point *p* is determined by the angle between the two lines tangential to the CDV. (b) In case of two CDV positions, the angular coverage α in the point *p* is the union of the coverage from the two CDVs. (c) An example of full angular coverage being achieved in this transaxial plane for a brain scan with four CDV positions. The circles indicate the CDVs and the orange line denotes the convex hull surrounding the CDVs.

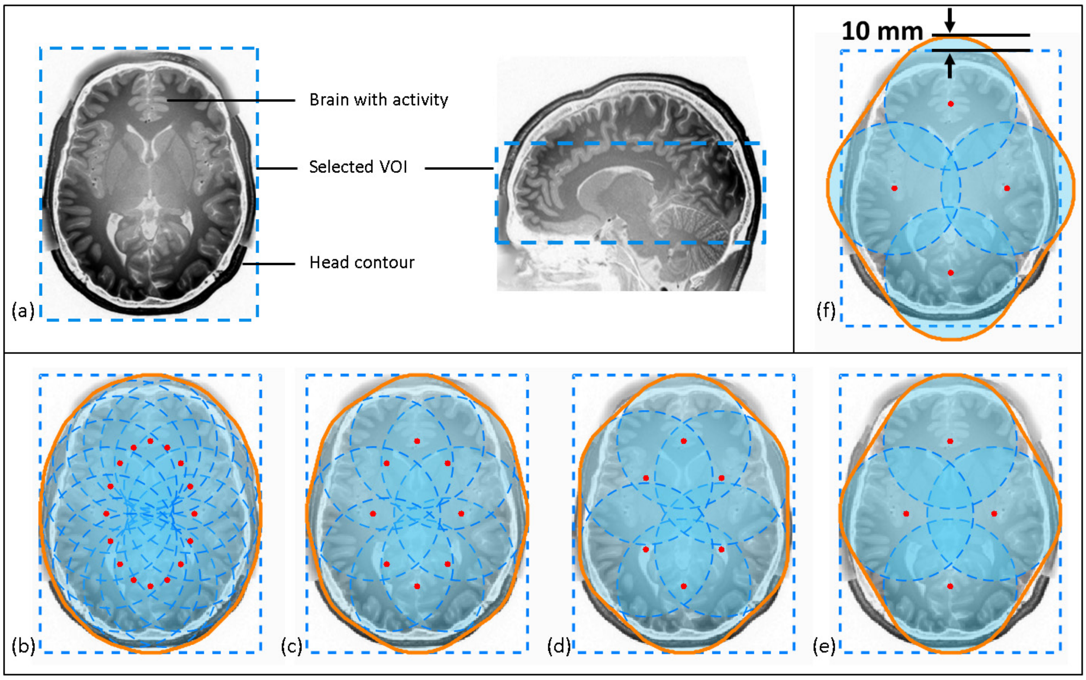

Figure 3. Illustration of VOI selection and the design of sampling sequences based on a set of MR scans. (a) Selection of the VOI based on the skull contour on an MR scan; (b)–(e) initial design of sampling sequences based on the selected VOI using 16, 8, 6 and 4 bed positions per transaxial plane. (f) Sampling sequence initially designed based on the skull contour is now shifted resulting in a convex skull 10 mm outside of the VOI. The dashed blue box is the selected VOI and the orange line indicates the corresponding convex hull. The bed positions are highlighted by the red dots that follow an elliptical trajectory. The semi-transparent blue circles with dashed blue edge are the CDVs at different bed positions.

60 mm, respectively. A precisely controlled 3D stage is incorporated for bed translations, enabling enlargement of the scan region. Scan region selection can be accomplished with the system's user interface that takes the images from three optical cameras as its input (figure 1(a)), see description in van der Have *et al* (2009) and Branderhorst *et al* (2011). The influence of intrinsic detector resolution (3.5 mm) is diminished by using a pinhole-detector distance (542 mm) that is larger than the object-pinhole distance (215 mm), such that projections are magnified onto the detector. Images from each pinhole are directly projected on the detectors. Shielding is placed between the pinhole and the detector to prevent overlapping projections. The inner diameter of the collimator is about 400 mm, making the system suitable for brain, selected extremity or pediatric imaging.

2.2. Convex hull principle

Sufficient sampling in the transaxial plane can be ensured by providing over 180° angular coverage for each point in the brain (Noo *et al* 2002, 2007, Chan *et al* 2016). As G-SPECT-I employs a multi-bed-position scan and uses the SFM which combines projections from different bed positions simultaneously into reconstruction, sufficient angular coverage is achieved when the brain is contained in the convex hull surrounding the CDVs from different scan positions. This is referred to as the convex hull principle and a demonstration of this principle is provided in figure 2. Figure 2(a) shows that the angular coverage α in the point p is determined by the angle between the two lines tangential to the CDV. Furthermore, figure 2(b) demonstrates that in case of two CDV positions, the angular coverage α in the point p is the union of the coverage from the two CDVs. Figure 2(c) gives an example of over 180° angular coverage being achieved in the transaxial plane for a brain scan with four CDV positions. The circles indicate the CDVs and the orange line denotes the convex hull surrounding the CDVs. Any point within the convex hull obtains an angular coverage of more than 180°.

2.3. Sampling sequence

As G-SPECT-I enables selection of the VOI that is to be scanned (via the user interface shown in figure 1), users can select the VOI based on the head contour on the optical images when performing a DaTscan, and the sampling sequence is then designed based on the selected VOI. Below we explain a general protocol for designing sampling sequences that should work on a variety of subjects. We aim to cover the entire brain in the convex hull with an extra minimal margin of 5 mm (minimal distance between the convex hull and the brain) for every subject in the test. This is to compensate for any mispositioning when selecting the VOI, and to make the protocol more applicable to all types of patients.

For our sampling sequence design, 30 brain MR scans were randomly selected from the HCP database (Hodge *et al* 2016) to check how one should position the bed transaxially once the head contour is known. First, a box (the selected VOI) was drawn manually on the transaxial plane based on the skull contour for each subject (as in figure 3(a)) with ImageJ (Schneider *et al* 2012). This box is selected to be just large enough to cover the head and this was checked by scrolling through all transaxial slices. Secondly, four sampling sequences with a reduced number of bed positions, from oversampling using 16 positions per plane, to 8, 6 and 4 were designed based on the selected VOI. All the transaxial sampling sequences follow elliptical trajectories. Initially these sequences were chosen such that the convex hull was just contained within the box as in figures 3(b)–(e). In figure 3, the dashed blue box is the selected VOI and the orange line highlights the convex hull. Then, we checked if the convex hull was large enough to cover the brain of all subjects with a minimal margin of 5 mm. When this was not the case, bed positions were shifted outwards to enlarge the convex hull as in the example of figure 3(f) where the bed positions are shifted resulting in a convex hull 10 mm outside the VOI box. We performed this procedure for all four sampling sequences on each subject, increasing the shift in steps of 1 mm, until the minimal margin of 5 mm was obtained for every subject. This way, we found that the sequences need to be shifted outwards by 0 mm, 2 mm, 5 mm and 15 mm when 16, 8, 6 and 4 bed positions were used, respectively. For clinical scans with G-SPECT-I, the VOI selection based on the optical images could be affected by scalp, hair, head support, etc. As a result, we would expect a slightly larger VOI than the one selected on the MR images, meaning that the minimal margin of 5 mm is a conservative estimation.

The above knowledge was subsequently applied in transaxial sequence design for a DaTscan with the Alderson phantom (RSD, USA). The VOI as indicated by the dashed blue box in figures 4(a)–(d) was selected based on the head contour of the phantom. The sampling sequences were then designed based on the selected VOI, taking the required shift according to MR scan findings into account.

For sufficient sampling along the axial direction, the transaxial bed positions are replicated. The required number of axial bed stops and distance between them are investigated. Firstly, as a reference, we start with a full brain scan with a large number of bed stops to be sure that sampling is more than sufficient. This scan with full brain oversampling uses seven axial bed stops as well as 16 bed positions per transaxial plane (thus a total of 112 bed positions is used). The distance between subsequent axial bed stops is set to 21 mm, which is small compared to the axial coverage L_c (60 mm) of each CDV.

To optimize the scanning length in axial direction, a reduced number of axial bed stops down to only one stop at the central position in the striatum is subsequently tested. The distance between consecutive axial bed stops remains 21 mm while oversampling is always ensured with 16 bed positions in the transaxial plane as performed in the reference image. This is to investigate whether projection truncation in the axial direction that occurs when the axial scan length is confined would induce artefacts. Meanwhile, transaxial sampling with fewer (8, 6 and 4 as in figure 4) bed stops is tested for each simulated scan with a set axial scanning length.

Additionally, to determine the optimal distance between axial bed positions, we increase the distance from 21 mm to 42 mm and to 60 mm (equal to the axial CDV length L_c). All the other procedures remain the same as implemented for 21 mm axial distance (i.e. gradually reducing the number of axial bed positions and testing with a reduced number of transaxial bed positions). All simulated scans are compared with the oversampled reference image.

2.4. Simulations

A digital phantom containing four striatum parts (left/right putamen and left/right caudate) was generated based on a CT image of the physical Alderson phantom. The remaining brain volume is the background compartment.

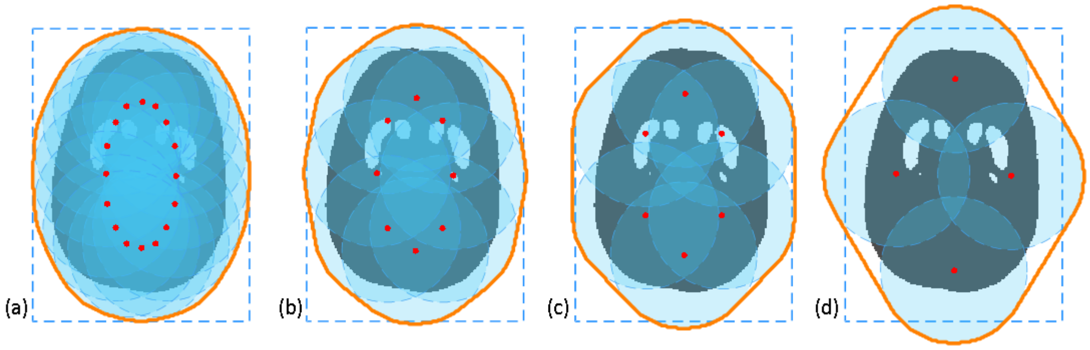

Figure 4. Transaxial sampling sequences used in this paper for a DaTscan of the Alderson phantom. Panels (a)–(d) show the sequences with 16, 8, 6 and 4 bed positions per transaxial plane as in figure 3, but with a shift of 0 mm, 2 mm, 5 mm and 15 mm, respectively based on the test results of the MR scans to contain the brain in the convex hull with a minimal margin of 5 mm.

Striatum-to-background concentration ratio is set to 8:1 to mimic a realistic distribution of ^{123}I-ioflupane (159 keV) in the brain. The emission process simulator is based on ^{99m}Tc (140 keV) point source measurements and geometry modeling (van der Have *et al* 2008). This approach of modeling low-energy isotope transport is also used when reconstructing experimental scans and has proven to provide good performance in many cases (Beekman *et al* 2005, van der Have *et al* 2009, 2016, Goorden *et al* 2013). Resolution is barely degraded when applied to isotopes with nearby peak energies (e.g. ^{111}In with photopeak of 171–245 keV (van der Have *et al* 2009) and ^{123}I with photopeak of 159 keV) compared to the scans with ^{99m}Tc. The phantom for projection has a voxel size of 0.75 mm, half the size of voxels in the reconstructed images, to mimic a continuous activity distribution. Both the projection simulation and reconstruction model the same physical effects, e.g. collimator attenuation, detector blurring, etc, and are derived from the same set of point source measurements. Besides, to make the simulation more realistic, phantom attenuation is modelled in the simulated projections using a voxelized ray tracer (Siddon 1985, Wang *et al* 2017). The attenuation map is derived by segmenting the CT image of the Alderson phantom, and assigning attenuation coefficients of 0 cm^{-1} to air, 0.15 cm^{-1} to soft tissue and 0.31 cm^{-1} to bone. Similarity-regulated OSEM (Vaissier *et al* 2016) with eight subsets and ten iterations is performed using SFM which combines projections from all bed positions simultaneously into image reconstruction. As we here aim to quantify errors induced only by sampling, no noise is simulated.

Moreover, to quantify the effects of different sampling strategies on the striatal count yield, a separate digital phantom with only the striatum was made by setting the tracer concentration in the background compartment to 0. The total striatal count for each sequence with reduced sampling is divided by that obtained with the reference scan. This way the gain of striatal count yield compared to that of the reference full brain oversampling is obtained.

2.5. Evaluation

As performed in clinical DaTscan assessment, visual inspection and semi-quantification of the DaTscan images are both included. The latter is achieved by calculating the specific binding ratio (SBR) and the asymmetry index (AI) in the left and right striatum, as well as the Localized SBR (L-SBR) and the Localized AI (L-AI) in eight striatal sub-regions. The definitions of the metrics are given by

$$SBR = \frac{C_{VOI\_str} - C_{VOI\_bkg}}{C_{VOI\_bkg}} \tag{1}$$

$$AI = 2 \times \frac{C_{RVOI\_str} - C_{LVOI\_str}}{C_{RVOI\_str} + C_{LVOI\_str}} \times 100\%. \tag{2}$$

Here C_{VOI_bkg} denotes the mean DaT image intensity in the background VOI. C_{VOI_str} represents the mean DaT image intensity within the striatal region, with C_{LVOI_str} and C_{RVOI_str} referring to the right and left part of striatum, respectively. While SBR and AI take values from the entire left or right striatum at one central slice as usually performed with traditional SPECT (figure 5(a)), L-SBR and L-AI give more detailed assessments in eight striatal sub-regions individually (figure 5(b)). These eight striatal VOIs, i.e. the posterior, middle and anterior putamen, and the caudate, for both the left and right striatum, are generated in PMOD v3.7 (PMOD Technologies Ltd., Switzerland) by placing small circles or ellipses over the putamen and caudate on the transaxial slices and are placed over 10.5 mm slices in the axial direction. The three parts of the putaminal VOIs have almost equal area on each transaxial slice. As there is no cerebellum or occipital cortex in the Alderson phantom, the background region is generated using the Southampton method (figure 5(c)) (Tossici-Bolt *et al* 2006). No filtering is applied on the phantom or the DaTscan images for the semi-quantification analysis to reduce partial volume effects.

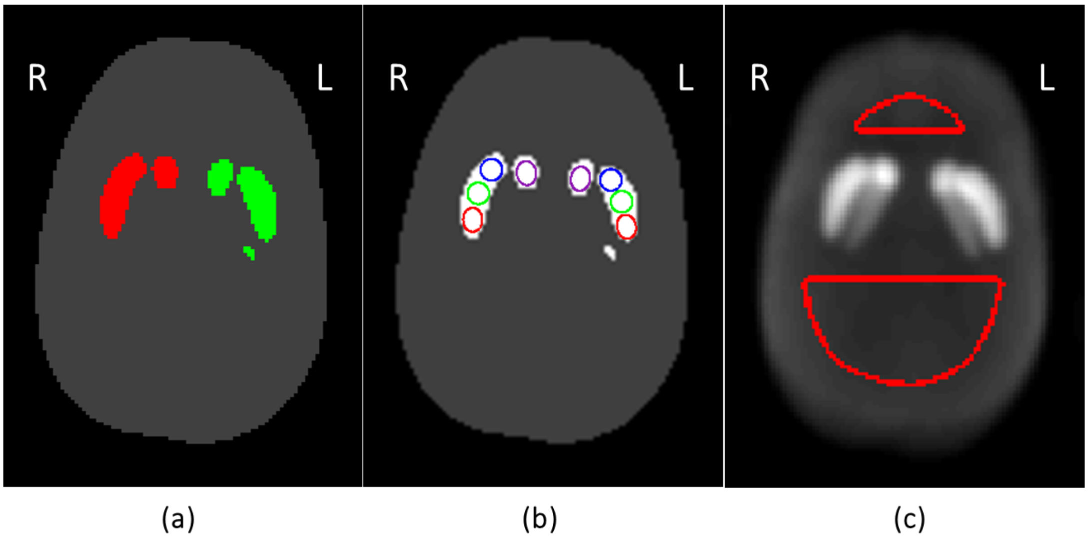

Figure 5. VOIs for semi-quantitative analysis. '*R*' and '*L*' indicate the right and left brain, respectively. (a) Striatum VOI taken from the phantom at the central slice of the striatum; (b) example of eight striatal VOIs on one transaxial slice; (c) background VOI generated using the Southampton method. In (a), the right and left striatum are denoted by the red and green shapes, respectively. In (b), the striatal VOIs consist of eight sub-regions that are indicated by circles or ellipses in different colors. Red, green, purple and blue ones denote the posterior, middle, anterior putamen and the caudate, respectively. The background VOI in (c) is composed of two parts highlighted by the red shapes.

As an additional quantitative measure of the image quality within the entire transaxial brain, the maximum undersampling error (MaxUSE) and average undersampling error (AvgUSE) are calculated. These two metrics are defined as the maximum and average relative difference of each reconstructed image from the oversampled reference image, respectively. The relative difference is expressed by:

$$\text{Difference}(i) = \frac{\text{Image}(i) - \text{Reference}(i)}{\text{Reference}(i)} \times 100\%$$

where *i* denotes the image voxel. All images are post filtered with a Gaussian filter of 4 mm full width at half maximum (FWHM) to suppress insignificant local fluctuations. Afterwards, the relative difference is calculated based on equation (3). As the relative differences can be either positive or negative, the absolute values are used for the calculation of MaxUSE and AvgUSE. Only the voxels within the brain are taken into account. Since the quantitative assessment of a DaTscan in a clinical setting is typically based on regions with the size of striatal structures (from 4 cm^3 to 12 cm^3 (Koch *et al* 2005, Tossici-Bolt *et al* 2006, Lange *et al* 2014)), we resized the Difference image from a voxel size of 1.5 mm to 10.5 × 10.5 × 9 mm. This gives cubic VOIs of about 1 cm^3, which are small enough to estimate relevant intensity deviations in the striatal structures

3. Results

3.1. Visual inspection

To illustrate the visual effect on DaTscan images when reducing the number of bed positions, figure 6 shows the gold standard (digital phantom), the reference reconstruction (simulated full brain oversampling scan), and three representative DaTscans acquired with a reduced number of bed positions. Five slices within an axial region of 36 mm that are most relevant to DaTscan inspection and quantification are displayed. The center of the striatum in axial direction is defined as 0 mm, while the slice 18 mm underneath or above the center is defined to be at −18 or 18 mm, respectively. Figure 6 demonstrates that reducing the number of bed positions from full brain oversampling to 16 positions hardly has a visual effect on DaTscan images. When further decreasing the number of bed positions, background homogeneity is somewhat degraded due to the presence of stripe artifacts. However, for the striatum and its sub-structures, the shapes are always preserved with no obvious distortions, even with the use of only four bed positions. A full overview of the DaTscan images for all the tested sampling sequences using one or two axial positions as well as their difference images from the reference scan are included in the appendix (figures A1–A4).

3.2. Semi-quantification

Tables 1 and 2 show the effect on SBR quantification when scanning with a reduced number of bed positions. For validation of the oversampled reference scan, the SBR and L-SBR from the phantom are included for comparison and are denoted as a Gold Standard SBR (GS-SBR) and GS-L-SBR, respectively, while those from the reference

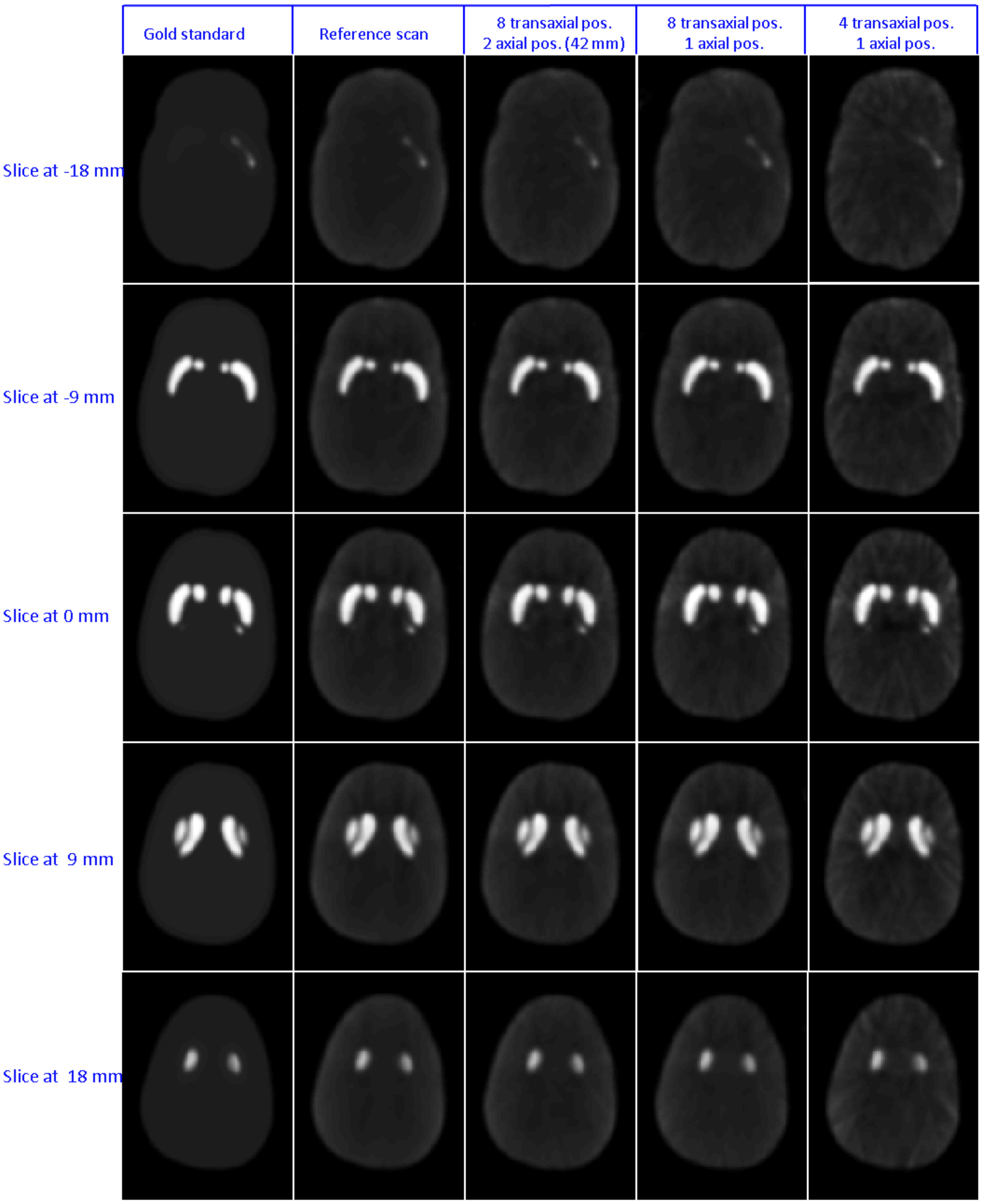

Figure 6. Comparison of the DaTscan image slices from the gold standard (the digital phantom), the reference scan (simulated full brain scan with oversampling), the DaTscan acquired with two axial positions combined with eight transaxial positions (distance between two axial positions is 42 mm), the scan with one axial position combined with eight transaxial positions, and the scan with one axial position combined with four transaxial positions. The center of the striatum in axial direction is defined to be at 0 mm. The top row to the bottom row represent the slices from 18 mm underneath the center of the striatum to 18 mm above it. All images have a pixel size and slice thickness of 1.5 mm and are post-filtered with a Gaussian filter of 4 mm FWHM. The concentration ratio in striatum and background compartment is 8:1. The Colormap is set from 0 to 8 (intensity normalized to that of the background compartment) for the gold standard images, and from 0 to 2.66 (the maximum intensity in the reference scan) for all the simulated DaTscan images. A full overview of the DaTscan images for all the tested sampling sequences using one or two axial positions as well as their difference images from the reference scan are included in the appendix.

scan are termed the Ref-SBR and Ref-L-SBR. Table 1 demonstrates that accurate SBR quantification can be achieved with the reference full brain oversampling. A maximum deviation of 3.1% and 6.3% in the posterior putamen and among all eight striatal sub-regions, respectively, are found when comparing the Ref-L-SBR with the GS-L-SBR. When decreasing the number of axial and/or transaxial bed positions from the oversampled reference scan, the effect on SBR quantification is very limited (table 2), which is demonstrated by a maximum deviation of 4.5% and 7.4% from the Ref-SBR and Ref-L-SBR, respectively, for all scans included in the table. Particularly, the mean deviation from the reference among all striatal sub-regions reads only 0.8% and 2.3% when using 16 positions (two axial positions and eight transaxial positions with a between stop distance of 42 mm) and four positions (one axial positions and four transaxial positions), respectively. The results for two

Table 1. Deviation between the reference scan and the GS in terms of SBR and L-SBR. Sub-regions are assessed separately. Post Put. = posterior putamen, Mid. Put. = middle putamen, Ante. Put. = anterior putamen. '*R*' and '*L*' indicate the right and left striatum, respectively. The deviation is calculated by subtracting the GS-SBR from the Ref-SBR and normalized by dividing by the GS-SBR. The same goes for the deviation of L-SBR. The absolute value of the deviations is used.

	L-SBR in eight sub-regions								SBR in striatum	
	Post. Put.		Mid. Put.		Ante. Put.		Caudate		Striatum	
Deviation from GS	*R* (%)	*L* (%)	*R* (%)	*L* (%)	*R* (%)	*L* (%)	*R* (%)	*L* (%)	*R* (%)	*L* (%)
Reference scan (112 pos.)	2.16	3.05	0.71	6.03	2.35	6.32	5.39	0.22	6.83	3.91

Table 2. Deviations from the Ref-SBR and Ref-L-SBR for scans with a reduced number of bed positions. The 21 mm and 42 mm in parenthesis in the first column indicate the distance between the two axial bed positions. Post Put. = posterior putamen, Mid. Put. = middle putamen, Ante. Put. = anterior putamen. '*R*' and '*L*' indicate the right and left striatum, respectively. The deviation is calculated by subtracting the Ref-SBR and normalized by dividing by the Ref-SBR. The same goes for the deviation of L-SBR. The absolute value of the deviations is used.

		L-SBR in eight sub-regions								SBR in striatum	
		Post. Put.		Mid. Put.		Ante. Put.		Caudate		Striatum	
Deviation from reference		*R* (%)	*L* (%)	*R* (%)	*L* (%)	*R* (%)	*L* (%)	*R* (%)	*L* (%)	*R* (%)	*L* (%)
One axial stop	16 transaxial pos.	0.74	3.08	4.53	4.28	1.15	3.91	6.17	5.04	4.53	3.57
	8 transaxial pos.	0.94	4.63	3.79	4.04	0.43	4.94	4.98	3.82	3.99	3.64
	6 transaxial pos.	3.58	6.58	0.89	1.46	0.13	3.52	0.41	2.77	2.43	3.34
	4 transaxial pos.	1.47	5.47	2.02	2.33	2.61	1.64	1.83	1.15	0.04	1.51
Two axial stops (21 mm)	16 transaxial pos.	2.32	2.35	3.32	2.03	3.19	3.17	3.64	2.88	2.94	2.94
	8 transaxial pos.	2.01	2.95	3.48	1.27	2.42	3.29	2.88	2.58	2.52	2.78
	6 transaxial pos.	3.30	3.32	0.64	0.74	1.89	1.88	0.30	0.19	1.07	1.70
	4 transaxial pos.	3.48	4.05	0.16	1.85	6.63	2.57	1.74	2.08	1.82	0.57
Two axial stops (42 mm)	16 transaxial pos.	0.64	0.23	0.22	0.23	1.24	0.66	1.11	0.24	1.47	0.27
	8 transaxial pos.	0.11	1.51	0.16	0.30	1.76	0.30	1.62	0.30	1.70	0.29
	6 transaxial pos.	1.14	0.27	0.17	0.64	1.63	1.94	2.83	1.56	2.45	0.23
	4 transaxial pos.	6.98	0.47	4.06	1.18	7.42	2.84	2.28	1.80	3.70	3.75

Table 3. Deviation between the reference scan and the GS in terms of AI and L-AI. The GS-L-AI and GS-AI are 0% as the intensity in the left or right striatum are all set to the same value in the phantom. The deviation from the GS-AI is calculated directly by subtracting the GS-AI (0%) from the Ref-AI, as AI is already a normalized index expressed in percentage. The absolute value of the deviations is given in the table. Post Put. = posterior putamen, Mid. Put. = middle putamen, Ante. Put. = anterior putamen.

	L-AI in eight sub-regions				AI in striatum
Deviation from GS	Post. Put. (%)	Mid. Put. (%)	Ante. Put. (%)	Caudate (%)	Striatum (%)
Reference scan (112 pos.)	0.05	3.13	4.54	6.28	2.77

axial bed positions with a distance of 60 mm between stops is not included, as it leads to diminished focus on the striatum and larger errors compared to 42 mm distance (see figures A3 and A4 in the appendix).

As another confirmation of the accurate SBR quantification for the tested sampling sequences, figure 7 directly shows the L-SBR values. As a benchmark, the GS-L-SBR is also shown by the dotted red line of L-SBR = 7 since the striatum-to-background concentration ratio is set to be 8:1.

Tables 3 and 4 show the effect on left-right asymmetry when scanning with reduced number of bed positions. The definitions of GS-AI, GS-L-AI, Ref-AI and Ref-L-AI which refer to phantom and reference scan values, are the same as for SBR, but consider the left-right asymmetry index. The GS-AI and GS-L-AI are 0% since the intensity in the left or right striatum are all set to the same value in the phantom. Table 3 manifests that a good left-right symmetry can be achieved with the oversampled reference scan. A maximum Ref-L-AI of 6.3% among all the striatal sub-regions is found. For the posterior putamen, the intensity in the left or right has an almost perfect match, resulting in an asymmetry of only 0.05%. Similar to the SBR results, decreasing the number of axial and/or transaxial bed positions has a limited effect on the left-right symmetry (table 4). The maximum deviation from the Ref-AI and Ref-L-AI is 2.4% and 7.0% in the striatum and among all eight striatal sub-regions, respectively, for all scans included in the table. Particularly, the mean deviation from the reference reads only 1.4% and 3.7%, respectively among all sub-regions when using 16 positions (two axial positions and eight transaxial positions with a between stop distance of 42 mm) and four positions (one axial positions and four transaxial positions).

Table 4. Deviations between the scan with a reduced number of bed positions and the reference scan in terms of AI and L-AI. This deviation is calculated by directly subtracting the Ref-AI, as AI is already a normalized index expressed in percentage. The absolute value of the deviations is given in the table. Post Put. = posterior putamen, Mid. Put. = middle putamen, Ante. Put. = anterior putamen.

		L-AI in eight sub-regions				AI in striatum
Deviation from reference		Post. Put. (%)	Mid. Put. (%)	Ante. Put. (%)	Caudate (%)	Striatum (%)
One axial stop	16 transaxial pos.	0.41	0.8	1.56	0.72	0.92
	8 transaxial pos.	0.50	0.30	1.14	0.21	0.34
	6 transaxial pos.	3.64	2.91	0.48	1.29	0.89
	4 transaxial pos.	4.10	6.98	0.18	3.46	1.45
Two axial stops (21 mm)	16 transaxial pos.	0.85	0.80	0.31	0.82	0.01
	8 transaxial pos.	0.40	0.33	0.59	1.29	0.25
	6 transaxial pos.	1.37	1.40	0.94	0.55	0.63
	4 transaxial pos.	3.32	6.57	1.56	3.93	2.40
Two axial stops (42 mm)	16 transaxial pos.	1.88	0.43	1.34	0.47	1.21
	8 transaxial pos.	1.89	1.80	1.80	0.00	1.43
	6 transaxial pos.	2.78	2.23	2.70	0.94	2.25
	4 transaxial pos.	0.48	3.35	1.84	2.98	0.05

Similar to figures 7 and 8 directly shows the L-AI values for scans with different sampling sequences. While the maximum L-AI for the reference scan is 6.3% among all striatal sub-regions, this value degrades only slightly to 7.6% for all scans included in the figure, confirming the good left-right symmetry even when scanning with reduced sampling. Besides, compared to a mean L-AI of 3.4% for the reference scan, comparable result of 3.0% and 3.8% is achieved for the scan with 16 positions (two axial positions and eight transaxial positions with a between stops distance of 42 mm) and the scan with 4 positions (one axial positions and four transaxial positions), respectively.

3.3. MaxUSE and AvgUSE

Table 5 summarizes the MaxUSE and AvgUSE for evaluation of the image quality in the entire transaxial plane when scanning with different sampling strategies. The values are calculated from those slices relevant for a DaTscan, along an axial length of 36 mm (−18 mm to 18 mm). This table shows that using a single bed position in axial direction results in a MaxUSE of 15.0%, 15.8%, 22.1%, 40.7% in relevant transaxial slices (−18 mm to 18 mm) when 16, 8, 6 and 4 transaxial bed positions are used respectively, while the AvgUSEs are all below 5.2% for the four sampling sequences. Besides, using two axial bed positions can improve both the MaxUSE and AvgUSE, while a 42 mm distance between axial stops gives the best accordance with the reference image compared to a 21 mm or 60 mm distance. For that separation, a MaxUSEs and AvgUSEs of 8.7% and 1.8%, respectively, could be achieved along 36 mm axial length when using 8 transaxial bed positions. These two values are only slightly affected (12.9% and 2.0%) when the axial length is extended to 90 mm (see the appendix). Increasing the number of transaxial bed positions from 8 to 16, the improvement of the results is limited.

3.4. Striatal count yield

Table 6 gives the quantitative measure of how much striatal counts can be gained compared to the reference full brain sampling when using a confined axial scanning length and different transaxial sequences. All count numbers are relative to the striatal count yield obtained with the reference scan. This table indicates that using a limited axial scanning length leads to a higher striatal count yield than full brain imaging. The maximal gain in striatal count yield is a factor 2.8 when only one axial bed stop is used, while 2.6, 1.9 and 1.0 times higher count yields are obtained with two axial bed positions at a distance of 21 mm, 42 mm and 60 mm, respectively. Meanwhile, the striatal count yield increases when more transaxial bed positions are applied. An increase of 10% is obtained when increasing the number of transaxial bed positions from 4 to 8. This is due to the fact that the sampling sequence can be more focused in the brain when more transaxial bed positions are used, while the whole brain is still contained in the convex hull (see figure 4).

4. Discussion

We investigated the effects of using different sampling strategies on visual image quality, semi-quantitative analysis accuracy, and striatal count yield for DaT imaging. By testing on a series of sampling sequences with a reduced number of bed stops, we found that the use of only four bed positions (one axial position combined with four transaxial positions) could already achieve very accurate semi-quantification. Compared to the oversampled reference scan, the deviation is only 1.5% for both the SBR and AI in the striatum, and 5.5% and 7.0% maximally

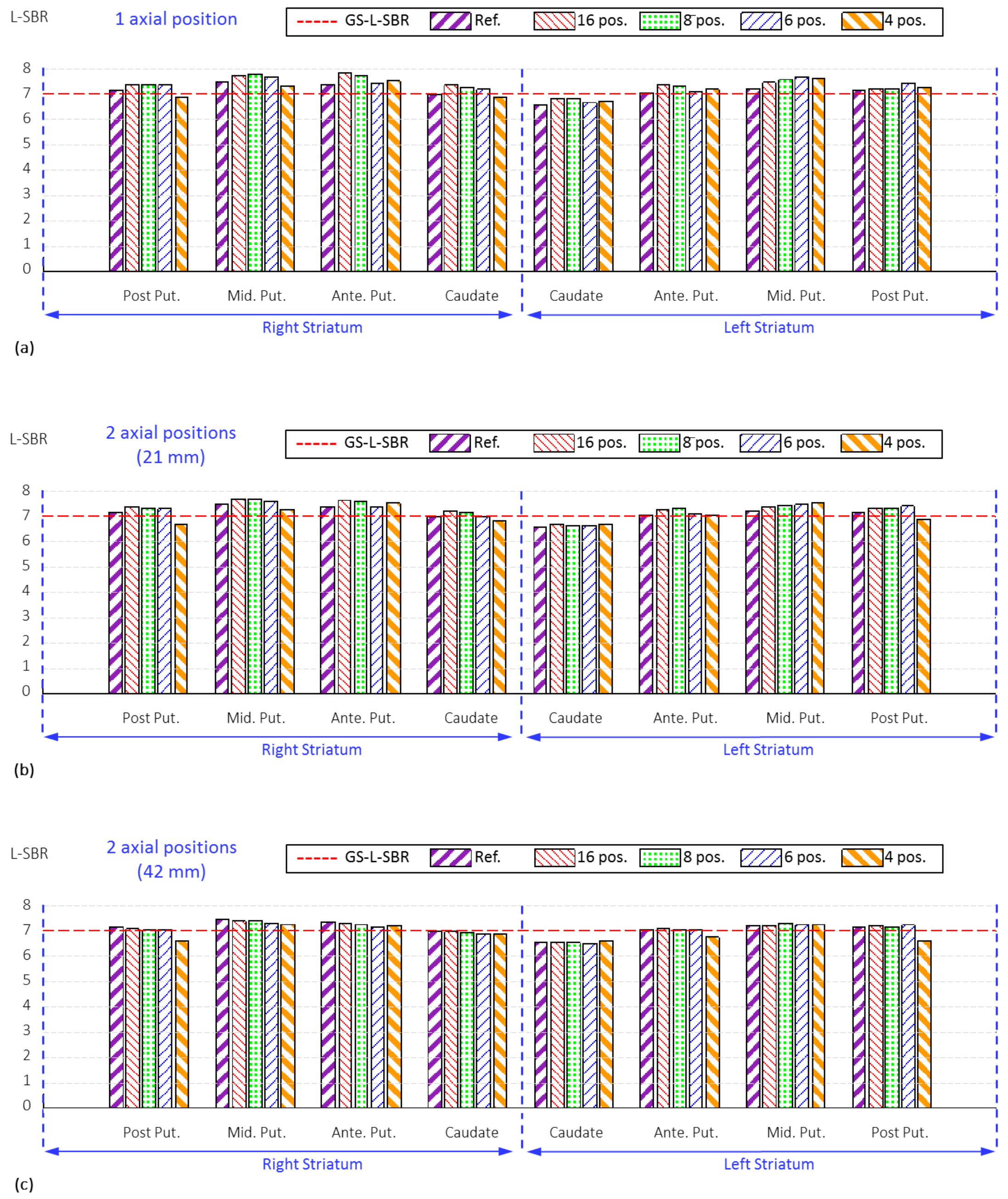

Figure 7. Comparison of the L-SBR for scans with different sampling sequences. The subplot at each row shows the results of (a) using one axial bed position, (b) using two axial bed positions with a between stops distance of 21 mm, and (c) using two axial bed positions with a between stops distance of 42 mm. Sub-regions of the striatum are assessed separately as in table 2. The GS-L-SBR is indicated by the dotted red line (L-SBR = 7, since the striatum-to-background concentration ratio is eight), while the Ref-L-SBR is denoted by 'Ref.' in the figure. The results of using different transaxial sampling sequences with 16, 8, 6 and 4 positions per plane are displayed in each subplot.

for L-SBR and L-AI among eight striatal sub-regions. Meanwhile, with the same sequence a striatal count yield of 2.5 times that of the reference full brain imaging could be achieved. However, due to the reduced sampling with less bed positions, the homogeneity in the background region is degraded, which leads to an MaxUSE of 40.1% at a few pixels. For a DaTscan, this might not be an important issue as structures essential for PD diagnosis are visually and quantitatively barely affected. However, for other types of scans such as brain perfusion scans, the affected homogeneity in the brain should be avoided.

As expected, the use of only a single axial bed position results in the highest striatal count gain (2.8 times that of the reference scan), since all bed positions are placed central to the striatum in the axial direction. Meanwhile, increasing the number of transaxial bed positions can also improve the number of detected striatal counts, owing to the more focused bed position placement in the brain (see figure 4 and table 6). For example, using eight transaxial positions leads to a 10% higher striatal count yield compared to utilizing four transaxial bed positions. It is worth noting that the total scan time is assumed to be the same for all simulated scans and the time for bed movements is not included in the simulation since it is highly dependent on the bed in use. Thus a slight decrease

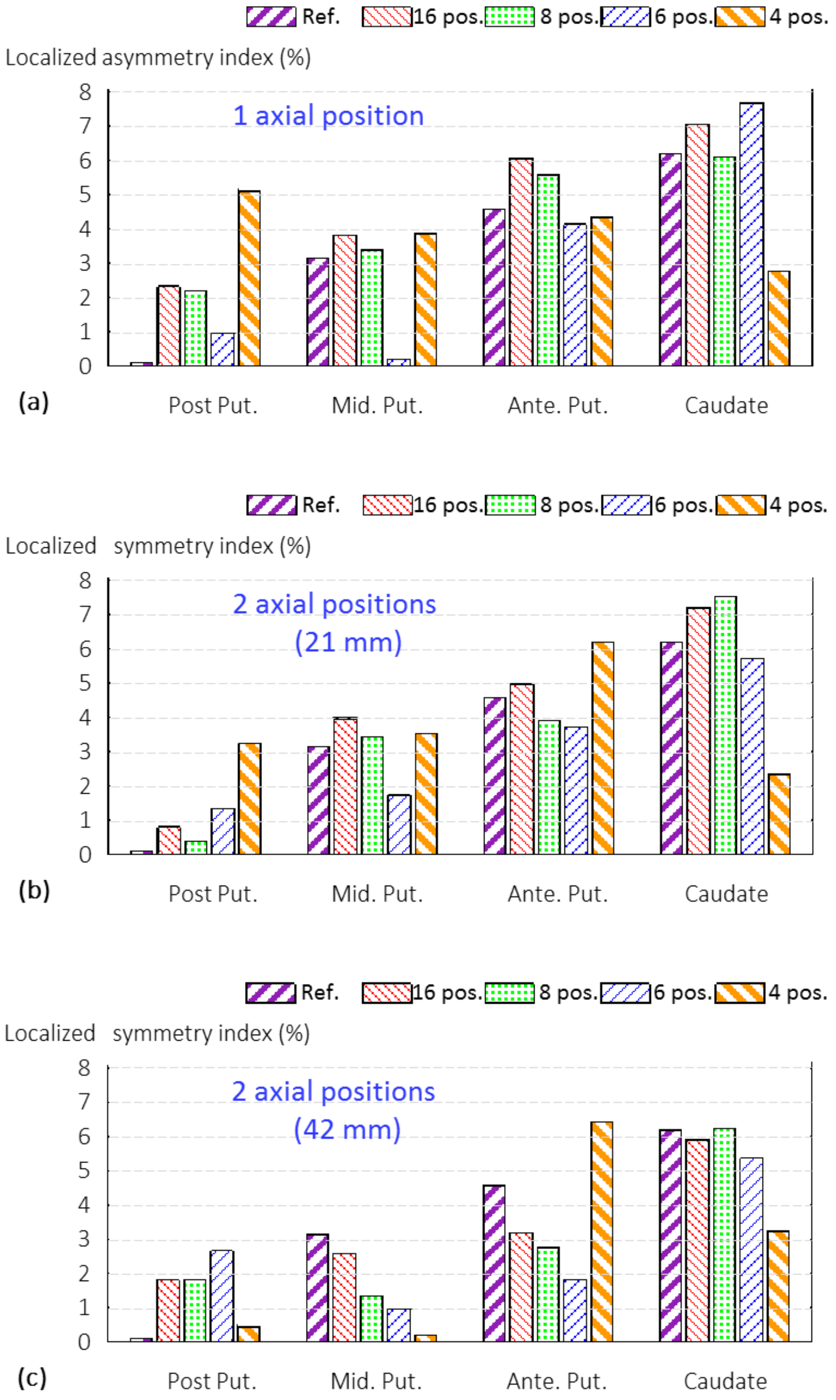

Figure 8. Localized asymmetry index results when using different sampling sequences. Assessment is performed in each sub-region. Post Put. = posterior putamen, Mid. Put. = middle putamen, Ante. Put. = anterior putamen. Note that the scale is from 0% to 8%.

of the striatal count yield would be expected when increasing the number of transaxial bed positions from 4 to 16 (e.g. two axial positions combined with eight transaxial positions) under equivalent total scan time if this overhead time would be taken into account. This favors the choice of using four bed positions (an overhead time of about 6 s based on our rough estimation using the current G-SPECT-I bed in design) for a multi-frame dynamic scan or fast scan. With the use of two axial positions combined with eight transaxial positions, the overhead time is estimated to be 24 s, which is still quite small compared to common acquisition times.

Note that here we aim to ensure an accurately reconstructed region of 35 mm in axial direction. Hence for clinical DaTscans, doctors who are familiar with DaTscan acquisition can select a VOI along an axial length of 35 mm. Determination of the striatum position could also be improved based on a brain MR database analysis that G-SPECT-I could provide. On the other hand, the scan region in axial direction can be extended by using more axial bed positions, which is shown by comparing the results of using one or two axial positions in the appendix (figures A1–A4). For the use of two axial positions combined with eight transaxial positions, the MaxUSE and AvgUSE are below 12.9% and 2.0%, respectively, along a 90 mm axial length, while very accurate semi-quantification results are still achievable (a deviation of 1.7% and 1.4% for the SBR and AI, respectively,

Table 5. Comparison of the MaxUSE and AvgUSE for scans with different sampling strategies in the transaxial slices relevant for a DaTscan, along an axial length of 36 mm (−18 mm to 18 mm).

		Number of transaxial bed positions			
MaxUSE along an axial length of 36 mm		4 (%)	6 (%)	8 (%)	16 (%)
One axial bed position		40.7	22.1	15.8	15.0
Two axial bed positions	21 mm distance	39.6	17.1	12.5	13.8
	42 mm distance	29.0	11.4	8.7	7.6
	60 mm distance	30.8	16.6	18.6	17.4
		Number of transaxial bed positions			
AvgUSE along an axial length of 36 mm		4 (%)	6 (%)	8 (%)	16 (%)
One axial bed position		5.2	3.4	3.2	3.6
Two axial bed positions	21 mm distance	4.6	2.9	2.4	2.5
	42 mm distance	4.0	2.6	1.8	1.2
	60 mm distance	5.0	4.0	3.5	3.4

Table 6. Comparison of the striatal count yield for scans with different sampling strategies. All count numbers are normalized by dividing by the striatal count yield achieved for full brain oversampling (sequence for reference scan).

		Number of transaxial bed positions			
Striatal count yield gain compared to full brain oversampling		4	6	8	16
One axial bed position		2.45	2.65	2.77	2.83
Two axial bed positions	21 mm distance	2.25	2.43	2.54	2.60
	42 mm distance	1.64	1.74	1.81	1.85
	60 mm distance	0.88	1.04	1.01	1.02

in the striatum, and 1.8% and 1.9% maximally for the L-SBR and L-AI among eight striatal sub-regions).Thus an extended axial region (e.g. 90 mm) could be selected to compensate for some mispositioning uncertainty (27 mm in both directions axially). As 90 mm is already much larger than the axial length of the reconstructable region aimed for (35 mm), more axial bed positions are not included.

We modelled attenuation using a voxelized ray tracer in the simulated projections. Attenuation correction is not performed for this study as it is not trivial with multi-pinhole systems and we aim to focus on sampling issues here. The reconstructed DaTscan images (figure 6) show that attenuation results in reduced intensities in the central part of the image, which is similar to what happens using parallel hole collimated SPECT systems. Nevertheless, the effect of different sampling sequences on G-SPECT-I DaTscan semi-quantification turns out to be not significant even with attenuation (figures 7 and 8 and tables 1–4).

5. Conclusion

We have designed and evaluated different sampling strategies for performing a DaTscan based on full G-SPECT-I simulations using measured system matrices. We find that structures essential for PD diagnosis were visually and quantitatively barely affected even when using four bed positions (a deviation of 1.5% for both the SBR and AI in the striatum, and 5.5% and 7.0% maximally for L-SBR and L-AI, respectively, among eight striatal sub-regions). With such a focused striatum scan, the effective count yield from the striatum increased by a factor of 2.5 compared to full brain imaging and much less overhead time is needed. This could enable acquisition with a total estimated overhead of bed-moving of only a few seconds and protocols for extremely fast dynamic brain SPECT and motion correction. Thus, the use of a limited number of bed positions does not significantly affect quantitative accuracy of a DaTscan while the striatal count yield is improved.

Acknowledgments

Financial disclosures of authors: FB and BV are employee and shareholder, and CW is an employee of MILabs. This work is part of the FOM Valorization Prize project ‘ultra-fast, ultra-sensitive and ultra-high resolution SPECT’ of the Netherlands Organization for Scientific Research (NWO). This research program is co-financed by MILabs BV.

Appendix

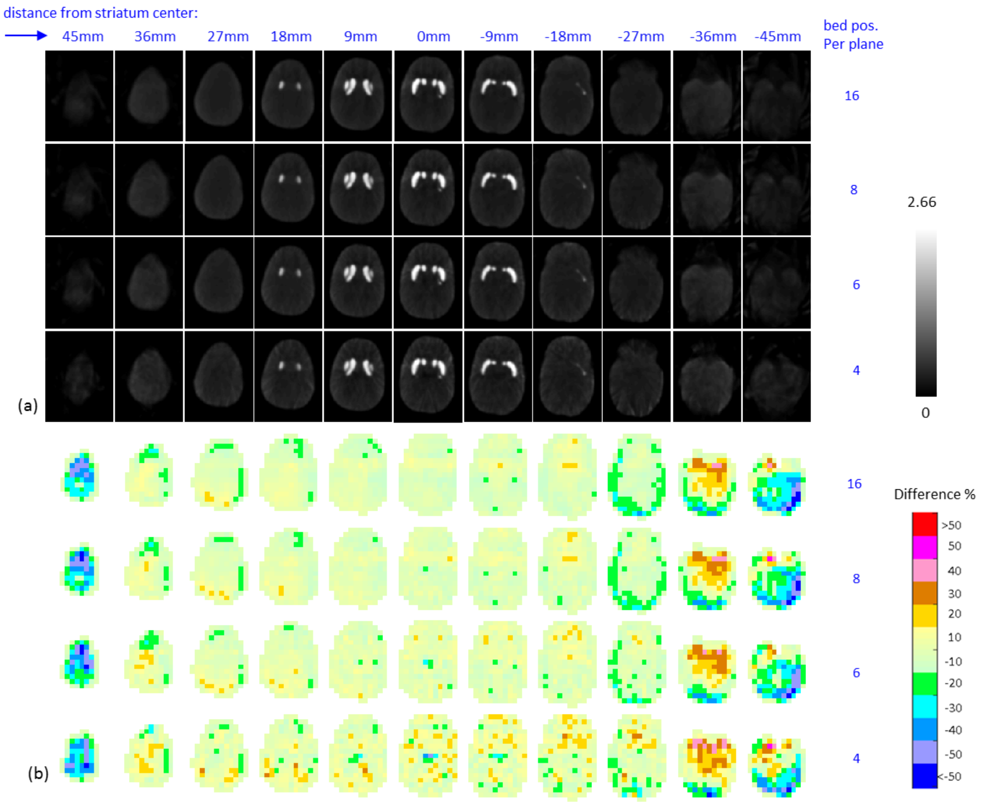

Figure A1. Comparison of simulated DaTscan images with the reference image when a single axial bed position is used. The single axial bed position is placed at the center of the striatum. (a) The simulated DaTscan image; (b) the Difference image calculated from the relative difference between the simulated DaTscan image in (a) and the reference image. Each row in (a) corresponds to one simulated scan, with the transaxial bed positions decreasing from 16, 8, 6 to 4 from the top to the bottom row, respectively. Images from left to right show the transaxial slices from 45 mm above the center of the striatum to 45 mm underneath it. The simulated DaTscan images in (a) have a pixel size and slice thickness of 1.5 mm and are filtered with a Gaussian filter of 4 mm FWHM. The Difference images in (b) have a pixel size of 10.5 mm and slice thickness of 9 mm.

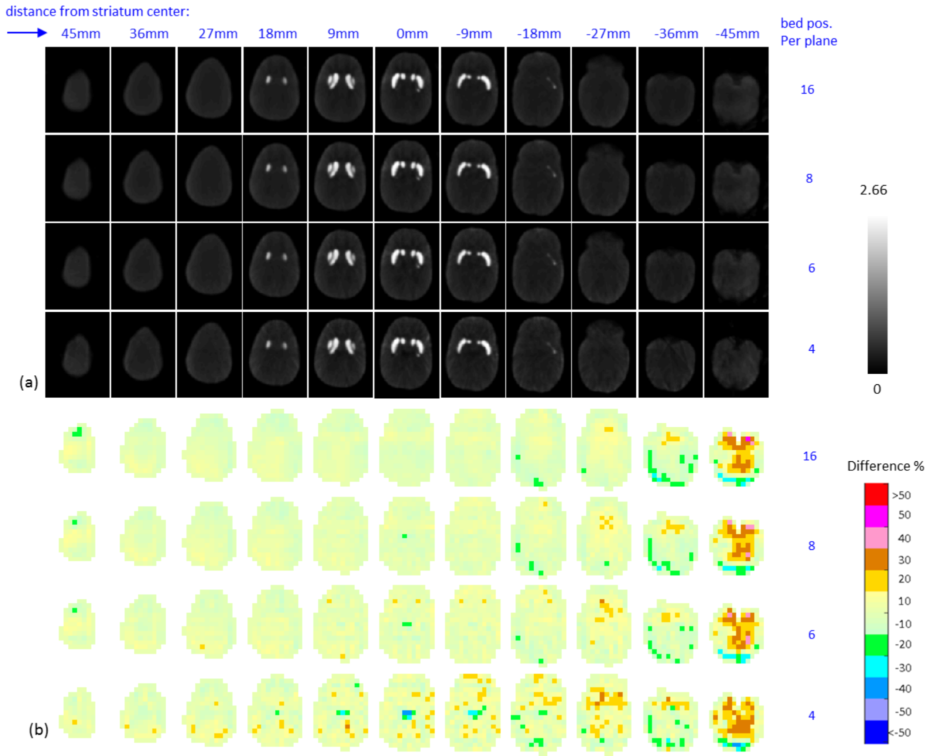

Figure A2. Like figure A1, but with two axial bed positions with a between stops distance of 21 mm.

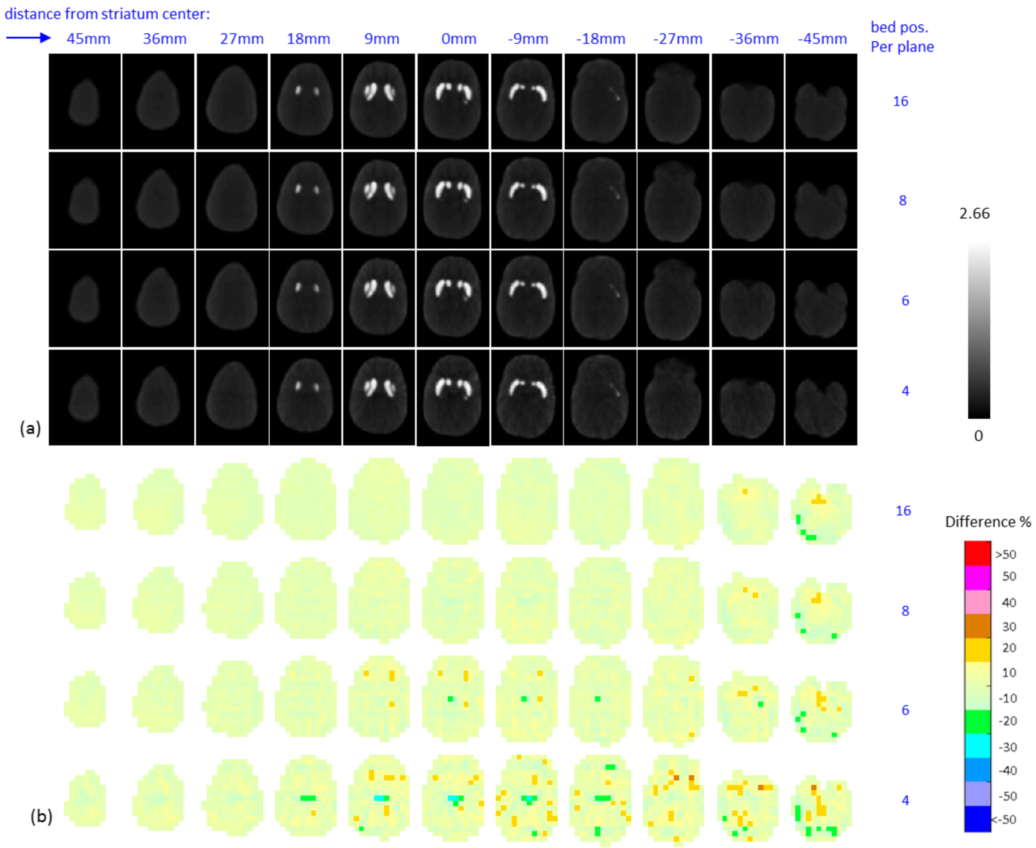

Figure A3. Like figure A1, but with two axial bed positions with a between stops distance of 42 mm.

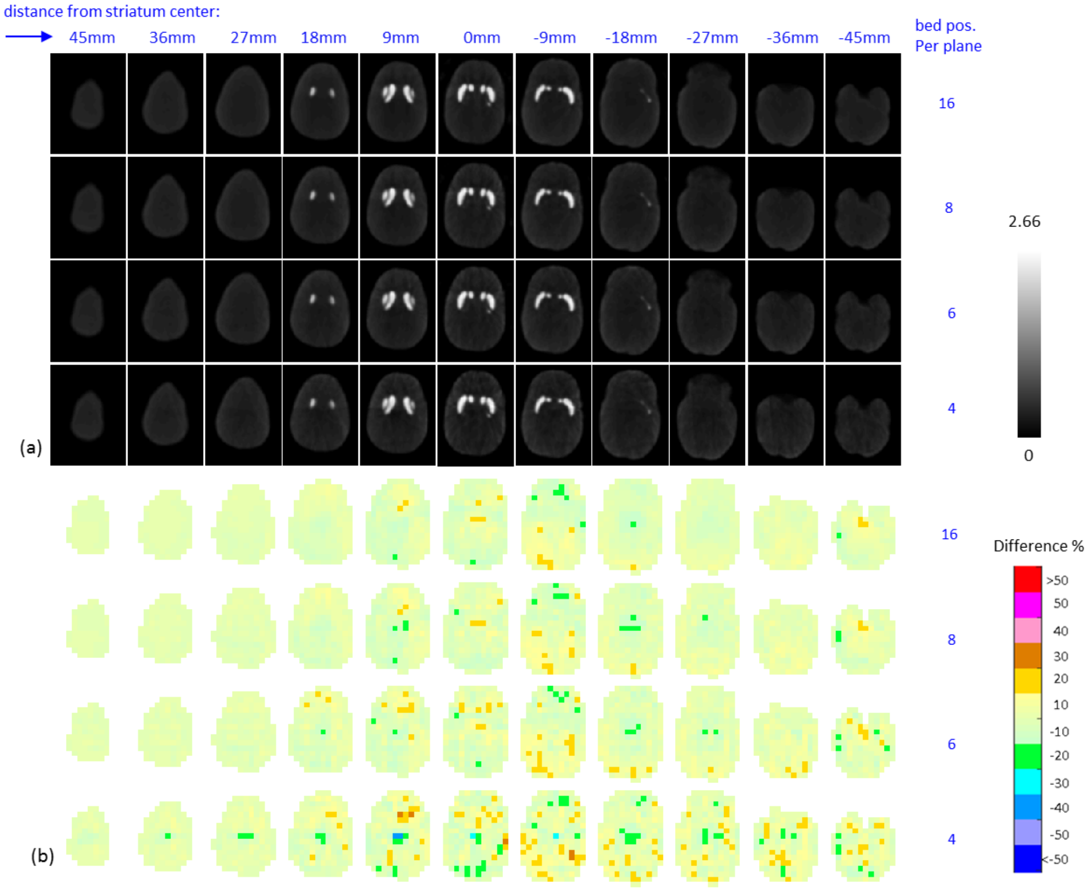

Figure A4. Like figure A1, but with two axial bed positions with a between stops distance of 60 mm.

References

Acton P D, Newberg A, Plössl K and Mozley P D 2006 Comparison of region-of-interest analysis and human observers in the diagnosis of Parkinson's disease using [^{99m}Tc]TRODAT-1 and SPECT *Phys. Med. Biol.* **51** 575–85

Augimeri A, Cherubini A, Cascini G L, Galea D, Caligiuri M E, Barbagallo G, Arabia G and Quattrone A 2016 CADA—computer-aided DaTSCAN analysis *EJNMMI Phys.* **3**

Bajaj N, Hauser R A and Grachev I D 2013 Clinical utility of dopamine transporter single photon emission CT (DaT-SPECT) with (^{123}I) ioflupane in diagnosis of parkinsonian syndromes *J. Neurol. Neurosurg. Psychiatry* **84** 1288–95

Beekman F J, van der Have F, Goorden M C, Vaissier P E B, van Roosmalen J, During H and Vastenhouw B 2015 G-SPECT-I: a full ring high sensitivity and ultra-fast clinical molecular imaging system with <3 mm resolution [abstract] *Eur. J. Nucl. Med. Mol. Imaging* **42** S209

Beekman F J, Van der Have F, Vastenhouw B, van der Linden A J, van Rijk P P, Burback J P H and Smidt M P 2005 U-SPECT-I: a novel system for submillimeter-resolution tomography with radiolabeled molecules in mice *J. Nucl. Med.* **46** 1194–200

Bombardieri E, Buscombe J, Lucugnani G and Schober O 2007 *Advances in Nuclear Oncology: Diagnosis and Therapy* (London: CRC Press) p 472

Branderhorst W, Vastenhouw B, Van Der Have F, Blezer E L A, Bleeker W K and Beekman F J 2011 Targeted multi-pinhole SPECT *Eur. J. Nucl. Med. Mol. Imaging* **38** 552–61

Catafau A M and Tolosa E 2004 Impact of dopamine transporter SPECT using ^{123}I-Ioflupane on diagnosis and management of patients with clinically uncertain parkinsonian syndromes *Mov. Disord.* **19** 1175–82

Chan C, Dey J, Grobshtein Y, Wu J, Liu Y-H, Lampert R, Sinusas A J and Liu C 2016 The impact of system matrix dimension on small FOV SPECT reconstruction with truncated projections *Med. Phys.* **43** 213–24

Chen L, Tsui B M W and Mok G S P 2017 Design and evaluation of two multi-pinhole collimators for brain SPECT *Ann. Nucl. Med.* **31** 636–48

De Deyn P 1997 *A Textbook of SPECT in Neurology and Psychiatry* (Libbey: John Libby Eurotext) p 128

Dierckx R, Otte A, de Vries E, van Waarde A and Paul L 2014 *PET and SPECT of Neurobiological Systems* (Berlin: Springer) p 238

Gayed I, Joseph U, Fanous M, Wan D, Schiess M, Ondo W and Won K-S 2015 The impact of DaTscan in the diagnosis of Parkinson disease *Clin. Nucl. Med.* **40** 390–3

Goorden M C, Rentmeester M C M and Beekman F J 2009 Theoretical analysis of multi-pinhole brain SPECT *Phys. Med. Biol.* **54** 6593–610

Goorden M C, van der Have F, Kreuger R, Ramakers R M, Vastenhouw B, Burbach J P H, Booij J, Molthoff C F M and Beekman F J 2013 VECTor: a preclinical imaging system for simultaneous submillimeter SPECT and PET *J. Nucl. Med.* **54** 306–12

Hammers A, Allom R, Koepp M J, Free S L, Myers R, Lemieux L, Mitchell T N, Brooks D J and Duncan J S 2003 Three-dimensional maximum probability atlas of the human brain, with particular reference to the temporal lobe *Hum. Brain Mapp.* **19** 224–47

Hauser R A and Grosset D G 2012 [^{123}I]FP-CIT (DaTscan) SPECT brain imaging in patients with suspected parkinsonian syndromes *J. Neuroimaging* **22** 225–30

Hodge M R *et al* 2016 ConnectomeDB—sharing human brain connectivity data *NeuroImage* **124** 1102–7

Ivashchenko O, van der Have F, Goorden M C, Ramakers R M and Beekman F J 2015a Ultra-high-sensitivity submillimeter mouse SPECT *J. Nucl. Med.* **56** 470–5

Ivashchenko O, van der Have F, Villena J L, Groen H C, Ramakers R M, Weinans H H and Beekman F J 2015b Quarter-millimeter-resolution molecular mouse imaging with U-SPECT^{+} *Mol. Imaging* **14** 7290–2014

Kawamura Y, Ashizaki M, Saida S and Sugimoto H 2008 Usefulness of rate of increase in SPECT counts in one-day method of N-isopropyl-4-iodoamphetamine [^{123}I] SPECT studies at rest and after acetazolamide challenge using a method for estimating time-dependent distribution at rest *Ann. Nucl. Med.* **22** 457–63

King M A, Mukherjee J M, Könik A, Zubal I G, Dey J and Licho R 2016 Design of a multi-pinhole collimator for I-123 DaTscan imaging on dual-headed SPECT systems in combination with a fan-beam collimator *IEEE Trans. Nucl. Sci.* **63** 90–7

Koch W, Radau P E, Hamann C and Tatsch K 2005 Clinical testing of an optimized software solution for an automated, observer-independent evaluation of dopamine transporter SPECT studies *J. Nucl. Med.* **46** 1109–18

Kouris K, Clarke G A, Jarritt P H, Townsend C E and Thomas S N 1993 Physical performance evaluation of the Toshiba GCA-9300A triple-headed system *J. Nucl. Med.* **34** 1778–89

Lange C *et al* 2014 CT-based attenuation correction in I-123-Ioflupane SPECT *PLoS One* **9** e108328

Lee T, Ellin J R, Huang Q, Shrestha U, Gullberg G T and Seo Y 2014 Multipinhole collimator with 20 apertures for a brain SPECT application *Med. Phys.* **41** 112501–7

Marzullo P, Mariani G and Kaufmann P 2013 *From Basic Cardiac Imaging to Image Fusion: Core Competencies Versus Technological Progress* (Berlin: Springer) p 56

Mukherjee J M, Dey J and King M A 2014 Image reconstruction methods for I-123 DaTscan imaging using a multi-pinhole and fan collimator dual-headed SPECT system *IEEE Nuclear Science Symp. and Medical Imaging Conf.* pp 1–3

Noo F, Defrise M, Clackdoyle R and Kudo H 2002 Image reconstruction from fan-beam projections on less than a short scan *Phys. Med. Biol.* **47** 2525–46

Noo F, Defrise M, Pack J D and Clackdoyle R 2007 Image reconstruction from truncated data in SPECT with uniform attenuation *Inverse Problems* **23** 645–67

O'Brien J T, Colloby S, Fenwick J, Williams E D, Firbank M, Burn D, Aarsland D and McKeith I G 2004 Dopamine transporter loss visualized with FP-CIT SPECT in the differential diagnosis of dementia with lewy bodies *Arch. Neurol.* **61** 919–25

Park E 2012 A new era of clinical dopamine transporter imaging using ^{123}I-FP-CIT *J. Nucl. Med. Technol.* **40** 222–8

PMOD 2017 PMOD software version 3.7 (www.pmod.com/web/)

Schneider C A, Rasband W S and Eliceiri K W 2012 NIH Image to ImageJ: 25 years of image analysis *Nat. Methods* **9** 671–5

Sensakovic W S, Hough M C and Kimbley El 2014 ACR testing of a dedicated head SPECT unit *J. Appl. Clin. Med. Phys.* **15** 1–10

Siddon R L 1985 Fast calculation of the exact radiological path for a three-dimensional CT array *Med. Phys.* **12** 252–5

Stoddart H A and Stoddart H F 1992 New multi-dimensional reconstructions for the lZdetector, scanned focal point, single-photon tomograph *Phys. Med. Biol.* **37** 579–86

Tavares A A *et al* 2013 *In vivo* evaluation of [^{123}I]MNI-420: A novel single photon emission computed tomography radiotracer for imaging of adenosine 2A receptors in brain *Nucl. Med. Biol.* **40** 403–9

Tossici-Bolt L, Hoffmann S M A, Kemp P M, Mehta R L and Fleming J S 2006 Quantification of [^{123}I]FP-CIT SPECT brain images: an accurate technique for measurement of the specific binding ratio *Eur. J. Nucl. Med. Mol. Imaging* **33** 1491–9

Vaissier P E B, Beekman F J and Goorden M C 2016 Similarity-regulation of OS-EM for accelerated SPECT reconstruction *Phys. Med. Biol.* **61** 4300–15

Van Audenhaege K, Van Holen R, Deprez K, Karp J S, Metzler S and Vandenberghe S 2011 Design of a static full-ring multi-pinhole collimator for brain SPECT *Nuclear Science Symp. and Medical Imaging Conf. (NSS/MIC)*

Van Audenhaege K, Van Holen R, Vanhove C and Vandenberghe S 2015 Collimator Design for a Multipinhole Brain SPECT Insert for MRI *Med. Phys.* **42** 6679–89

Van Audenhaege K, Vandenberghe S, Deprez K, Vandeghinste B and Van Holen R 2013 Design and simulation of a full-ring multi-lofthole collimator for brain SPECT *Phys. Med. Biol.* **58** 6317–36

Van De Giessen E and Booij J 2010 The SPECT tracer [^{123}I]ADAM binds selectively to serotonin transporters: a double-blind, placebo-controlled study in healthy young men *Eur. J. Nucl. Med. Mol. Imaging* **37** 1507–11

van der Have F, Ivashchenko O, Goorden M C, Ramakers R M and Beekman F J 2016 High-resolution clustered pinhole ^{131}Iodine SPECT imaging in mice *Nucl. Med. Biol.* **43** 506–11

van der Have F, Vastenhouw B, Ramakers R M, Branderhorst W, Krah J O, Ji C, Staelens S G and Beekman F J 2009 U-SPECT-II: an ultra-high-resolution device for molecular small-animal imaging *J. Nucl. Med.* **50** 599–605

van der Have F, Vastenhouw B, Rentmeester M C M and Beekman F J 2008 System calibration and statistical image reconstruction for ultra-high resolution stationary pinhole SPECT *IEEE Trans. Med. Imaging* **27** 960–71

Vastenhouw B and Beekman F 2007 Submillimeter total-body murine imaging with U-SPECT-I *J. Nucl. Med.* **48** 487–93

Wang B, Van Roosmalen J, Piët L, VanSchie M A, Beekman F J and Goorden M C 2017 Voxelized ray-tracing simulation dedicated to multi-pinhole molecular breast tomosynthesis *Biomed. Phys. Eng. Express* **3** 045021